Research Article Vol. 57, No. 18 / 20 June 2018 / Applied Optics 5019

applied optics

Compressed sensing hyperspectral imaging in the 0.9–2.5 μm shortwave infrared wavelength range using a digital micromirror device and InGaAs linear array detector

Md Masud Parvez Arnob,[1] Hung Nguyen,[1] Zhu Han,[1] and Wei-Chuan Shih[1,2,3,4,*]

[1]Department of Electrical and Computer Engineering, University of Houston, Houston, Texas 77204, USA
[2]Department of Biomedical Engineering, University of Houston, Houston, Texas 77204, USA
[3]Department of Chemistry, University of Houston, Houston, Texas 77204, USA
[4]Program of Materials Science and Engineering, University of Houston, Houston, Texas 77204, USA
*Corresponding author: wshih@uh.edu

Received 21 March 2018; revised 25 April 2018; accepted 17 May 2018; posted 17 May 2018 (Doc. ID 326328); published 12 June 2018

A hyperspectral imaging system based on compressed sensing has been developed to image in the 0.9–2.5 μm shortwave infrared wavelengths. With a programmable digital micromirror device utilized as spatial light modulator, we have successfully performed spectrally resolved image reconstruction with a 256-element InGaAs linear array detector without traditional raster scanning or a push-broom mechanism by a compressed sensing (CS) single-pixel camera approach. The chemical sensitivity of the imaging sensor to near-infrared (NIR) overtone signatures of hydrocarbons was demonstrated using hydrocarbon and ink patterns on glass, showing spectral selectivity for the chemical components. Compared to point-by-point raster scanning, we show that the CS scheme can effectively accelerate image acquisition with lower but reasonable quality.

OCIS codes: (110.4234) Multispectral and hyperspectral imaging; (300.6340) Spectroscopy, infrared; (110.1758) Computational imaging.

https://doi.org/10.1364/AO.57.005019

1. INTRODUCTION

Shortwave infrared (SWIR), or near-infrared (NIR), hyperspectral imaging is an effective technique to obtain spatially resolved molecular overtones and combination bands of fundamental molecular vibrational modes. SWIR/NIR spectroscopy and hyperspectral imaging has been widely adopted in pharmaceuticals [1], agricultural [2], cosmetics [3], medical [4,5], and petrochemical applications [6]. Hyperspectral imaging sensors often require a scanning mechanism to acquire individual pixels or entire lines of pixels sequentially. When the sensor is in motion, scanning can be implemented either as a raster-scan (point-scan) or "push broom" (line-scan) scheme. When the sensor is stationary, the point- or line-scan mechanisms typically employ optomechanical components such as galvomirrors [7]. An alternative scanning mechanism for stationary sensors is the use of a digital micromirror device (DMD) spatial light modulator, which has gained attention in quantitative spectroscopic applications [8,9]. Owing to the negligible mass of each micromirror, the DMD can operate at very fast frame rates. The DMD is a prominent example of a microelectromechanical system (MEMS) fabricated by integrated circuit (IC) technology, facilitating the implementation of a lightweight system for *in situ* field measurements. The high switching rate of the DMD has enabled fast acquisition for quantitative determination of analytical elemental composition, surface topography, and spectral imaging [9–11]. In the literature, a DMD has been employed in modern SWIR/NIR spectroscopy. Xiang *et al.* implemented a Hadamard transform NIR spectroscopy system using the DMD for glucose and lactate sensing with a single-element photodiode detector [8]. Fowler *et al.* proposed whiskbroom and pushbroom mechanisms in DMD illumination for possible applications in remote unispectral imaging [12]. Chen *et al.* constructed a DMD-based unispectral imaging sensor for capturing high resolution NIR images at a video rate [11]. To date, DMD-based hyperspectral sensors have not been demonstrated for the detection and identification of NIR molecular vibration.

Computational approaches to hyperspectral image reconstruction have been reported, showing benefits for faster data acquisition by significantly reducing the required number of measurements [13–15]. Duarte *et al.* introduced a new

imaging approach using a single-pixel camera where the compressed sensing (CS) theory is applied [16,17]. This imaging scheme involves multiplexed illumination where a DMD array illuminates the object simultaneously at different locations by random light modulation. The compressed sensing reconstruction requires at least a single element detector to record illumination data, removing the need for expensive array detectors. Other recent studies that incorporated the single-pixel camera approach for the NIR wavelength range were focused on image recovery [11,14,15] instead of combined instrument and algorithm design. The characterization of the CS method for molecular overtone detection for chemical sensing applications needs to be addressed to take advantage of the faster and sensitive SWIR/NIR hyperspectral imaging without the high costs of large format pixel array detectors. Moreover, we expect the hyperspectral imaging system to be useful in numerous applications that require increased molecular sensitivity and shorter acquisition times for hydrocarbons in the SWIR/NIR overtone region. The instrumentation is expected to be highly flexible for different applications of molecular sensing in the pharmaceuticals, agricultural, biomedical, and petrochemical industries.

Herein, we describe the SWIR/NIR hyperspectral instrumentation comprising a dispersive spectrograph combination of a DMD and an InGaAs linear array detector. Then, by incorporating CS image reconstruction methods involving the single-pixel camera technique, the effects on the acquisition time for sensitive SWIR/NIR hyperspectral imaging of hydrocarbons is evaluated with respect to number of CS measurements and, consequently, compared to the results of raster-scanning method using the DMD array. Finally, we present a practical demonstration of the CS image reconstruction for the chemical imaging of patterned hydrocarbon targets and petroleum samples.

2. MATERIALS AND METHODS

A. System Design and Implementation

The schematic diagram of the DMD-based SWIR/NIR hyperspectral imaging sensor is illustrated in Fig. 1. Collimated white light illuminates the scene, which is imaged on the DLP 9500 DMD using a $4f$ lens imaging system. Here, the scene is demagnified by two-thirds when imaged on the DMD array plane. The DMD array consists of optomechanical elements that redirects into two positions that determine the direction where the light is deflected, thereby acting as a spatial light modulator. The DMD mirrors can be oriented in one of two directions; −12° or +12° from the normal direction. The orientation of the mirror can be switched from one state to the other, enabling modulation of incident light with very high precision. In most recent reports, the DMD array was used only to screen spectrally dispersed light from the reflection diffraction grating [8,18]. Here, the light collected from a distant scene is imaged on a focal plane that coincides with the DMD array. The DMD array processes the spatially dispersed light from the sample scene. The DMD selects specific spatial regions from the sample scene to be imaged to the detector by projecting a predetermined sequence of micromirror patterns set in the "on" position.

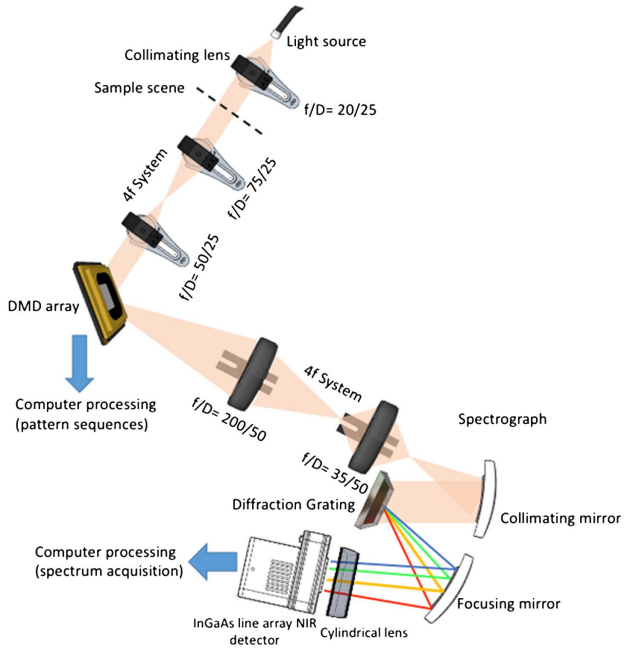

Fig. 1. Schematic diagram of the optical layout of the DMD-based SWIR/NIR hyperspectral image sensor.

In other words, the DMD array here acts as a light modulator of the spatial coordinates of the sample scene before being processed for spectral detection. Upon light entry to the dispersive spectrograph, instant capture of spectral information is enabled per detector acquisition. The light reflected from the "on" position of the DMD array is imaged using another $4f$ lens system with ∼5.7 times demagnification onto the entrance plane of the spectrograph. On the other hand, light reflected in the "off" position is deflected off the direction of the detection arm of the sensor. The image plane is collimated using a 150-mm focal-length curved mirror onto a plane-ruled reflection diffraction grating blazed at 1.71 μm with 75 grooves/mm density. Another 150-mm focal-length curved mirror refocuses the spectrally dispersed image for detection. A plano-convex cylindrical lens further demagnifies (5 times) the image in parallel into the length of the line array of the InGaAs detector. This design implementation uses no entrance slit but instead uses the dimensions of the encoded image plane from the DMD array to define the wavelength resolution. The width of the DMD pattern defines the spectral resolution across the line detector. The dimensions of the DMD spatial mask are defined by the number of micromirror pixels set in the "on" position. Each DMD micromirror is a square pixel (with 10.8 μm width). Finally, each pixel of the linear detector array records a narrow spectral range dispersed from the diffraction grating. The G9206-256W Hamamatsu line detector provides an array of 256 pixels with the following pixel dimensions: 250 μm height and 50 μm pitch. When 25 DMD pixels are used as one imaging superpixel (270 μm), the 5.7 times demagnification shrinks it down to 47 μm at the entrance plane of the spectrograph. This design is to match the InGaAs pixel size (50 μm). The grating linear dispersion for the spectrograph is $\sim 10^6/(150 \times 75) = 89$ nm/mm, yielding a spectral

resolution of $89 \times 0.05 = 4.4$ nm. The spectral resolution depends on several factors: number of DMD pixels in a super-pixel, DMD pixel size, demagnification, linear dispersion of spectrograph, and InGaAs pixel size. The spectral bandwidth afforded by the system depends on the spectral resolution and the number of pixels of the InGaAs array. In our implementation, the spectral range is $\sim 4.4 \times 256 = 1138$ nm.

B. System Characterization

Here we first demonstrate the spectral sensitivity of the instrument to the NIR overtone bands. Carbon–hydrogen (C–H) bonds, hydroxyl groups, aromatics, carboxyls (C=O), and other organic structural groups exhibit fundamental vibrations within the 2500–25,000 nm interval. These organic molecules also exhibit overtones and combination tones in the visible-NIR interval (500–2500 nm) [19]. In Fig. 2, the wavelength calibration was carried out by measuring the transmission curve for dichloromethane, a liquid calibration standard widely used for both transmission and reflectance modes [20]. The characteristic sharp bands for dichloromethane are labeled in Fig. 2A. The transmission curves of typical hydrocarbons found in fuel samples within the 1000–2000 nm interval measured using the hyperspectral sensor are also shown in Figs. 2B–2D. The first and second C–H overtones within the 1100–1800 nm window differs largely for each of the liquid hydrocarbons. In this experiment that the DMD array was used as a static mirror with a fixed set of micromirrors set at "on" position (a DMD array with 25×25 pixel dimension). The DMD array served as a controllable entrance slit for the SWIR/NIR spectrograph, resulting in the spectral resolution represented by the sharp overtone peaks (i.e., second C–H overtone and first C–H overtone bands of dichloromethane at 1150 and 1400 nm, respectively) in Fig. 2A. The overtone bands were also measured for typical liquid hydrocarbons such as ethanol, hexadecane, and iso-octanol (Figs. 2B–2D). The sharpness of the overtone bands varies for each spectrum, demonstrating the ability of the SWIR/NIR sensor to distinguish characteristic vibrational signatures of various hydrocarbons.

Next, to test the imaging capabilities of the hyperspectral sensor for hydrocarbon samples, a raster-scanning method is employed where single DMD pixel groups (with a fixed number of pixels) were turned on sequentially (while all others were off) to record the local transmission spectra of hydrocarbon constituents from a dried crude oil (Louisiana sweet grade) sample from specified spatial locations on a glass substrate (Figs. 2E–2H). The three regions marked as boxes 1–3 in Fig. 2E represent sample locations with different hydrocarbon NIR spectral signatures. The heterogeneity of the crude oil sample with the field of view (FOV) is demonstrated in terms of absorption intensity maps at 1210 and 1490 nm as shown in Figs. 2G and 2H, respectively. The raster-scanned maps were reconstructed from each region of interest (ROI), resulting in a slow data acquisition process. Aside from the lengthy raster-scanning procedures, various drifts during the data acquisition decreases the measurement stability (i.e., susceptible to time-sensitive changes in instrumental and sample conditions) of the system.

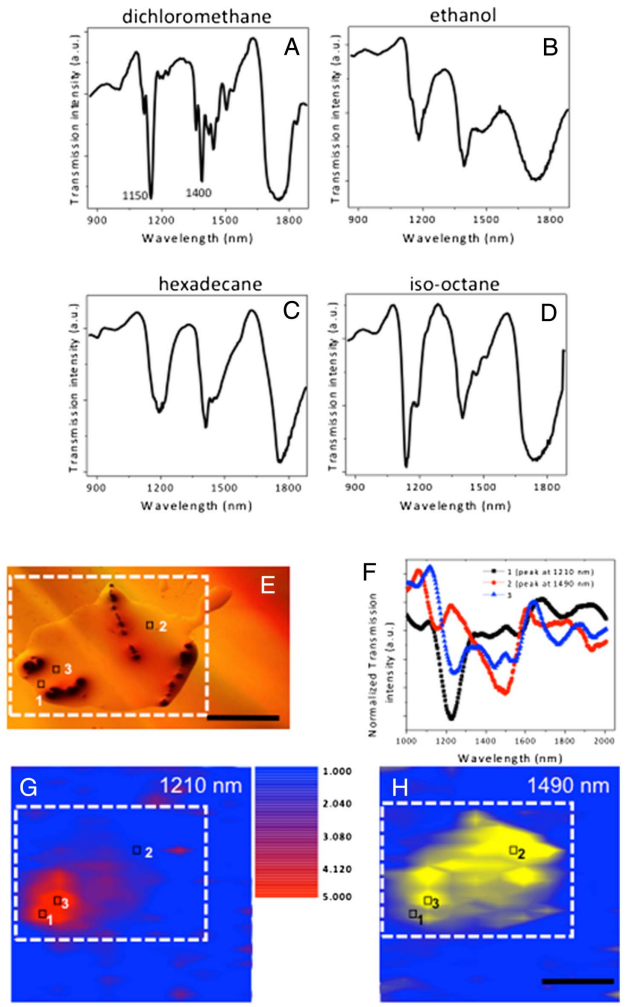

Fig. 2. Transmission curves for hydrocarbon solvents: A—dichloromethane (calibration standard), B—ethanol, C—hexadecane, and D—iso-octane. Point-by-point raster-scan imaging of oil film on glass. E—Brightfield microscope image of crude oil sample. F—Average transmission spectrum of different sample regions labeled 1–3. G—Absorption amplitude map (peak at 1210 nm) of image A. H—Peak amplitude map (peak at 1490 nm) of image A. Scale bar is 500 μm.

C. Compressed Sensing Methods

To address the inefficiencies of lengthy raster-scan measurements, we chose to incorporate the single-pixel camera imaging approach to the instrumentation [16,17]. From the previous measurements, we have performed only the raster-scanning methodology via DMD modulation where each single-pixel sensor of a 256-element detector takes N light measurements that represent intensity at specified sample coordinate. To streamline the data collection via multiplexed light modulation, image reconstruction using the compressed sensing algorithms can be employed. CS is an emerging methodology that has attracted intensive research activities in digital signal processing [21]. Compared to traditional sensing where a signal is first acquired then compressed, CS compresses a signal before it is recorded. This new sensing paradigm senses the information of the signal instead of the signal itself, and enables a potentially

large reduction in the sampling and computation costs for sensing signals that have a sparse or compressible representation (possible under a certain sparsifying basis) [22]. We have employed standard convex programming for $\ell 1$ minimization, something that has been utilized in the context of sparse solution for many years [22].

In our specific application, we treat an image by vectorizing it into a long 1D vector. Consider an image of N pixels represented by a vector $x \in \mathbb{R}^N$, with N elements $x[n]$, $n = 1, 2, \ldots, N$. A compressive digital camera is able to directly acquire $M < N$ random linear measurements without collecting the N pixel values individually. For each measurement $y[m]$, the compressive digital camera sets the mirror orientations in a pseudorandom 1/0 pattern to create the measurement vector A_m (row of matrix A) and measure the inner product $y[m] = (\mathbf{x}, A_m)$. The images are reconstructed using total variation minimization, which is closely related to wavelet coefficient $\ell 1$ minimization [23].

By treating each detector pixel on the InGaAs line array as a single-pixel camera [16,17], spatial information is simultaneously measured for each pixel using a pseudorandom sequence of binary (1/0) DMD patterns projected from the sample scene. The sequenced data is then used to reconstruct the hyperspectral cube that contains both spectral (dictated by the spectral information measured by each detector pixel) and dimensional (acquired with each DMD binary mask) information of the hydrocarbon sample. In the CS-mediated measurements, a single-pixel detector takes $M \leq N$ light measurements at a specified sequence using different combinations of the N pixels governed by a pseudorandom binary (0/1) test function. The scene is then reconstructed at the same resolution as the randomized masks on the DMD (i.e., $N = a \times b = 32 \times 32 = 1024$ elements) using a total-variation (TV) regularized reconstruction algorithm as thoroughly employed in single-pixel camera studies [11,16,17]. Each element of the binary pattern comprises a DMD pixel square array with a total of 64 pixels (a square array with 8 pixels on each side).

3. RESULTS AND DISCUSSION

Initially, we investigate the capability of the system by resolving an image of a sharp edge using a dark mask to block transmission of half of the FOV. For each measurement, the DMD projects a random binary spatial pattern, and the 256-pixel linear sensor records the spectrally diffracted linear image. An exposure duration of 4 ms for each acquisition (averaged from a total of 50 scans) was employed for each randomized mask from the DMD. To analyze the impact of the number of measurements (compression rate), the images were reconstructed using a pattern recovery with certain M number of measurements ($0.1N \leq M \leq 0.4N$). In other words, this would be equivalent to 10%–40% of the total of 1024 measurements for a complete raster scanning of an entire 32×32 element FOV. In Fig. 3A, the reconstructed images are presented at different compression rates (10%–40% pattern recovery). The results from the dark mask suggest that high-resolution images can already be recovered from a few randomized sets of multiplexed illumination. As expected, the imaging quality of the reconstructed images varies for each compression

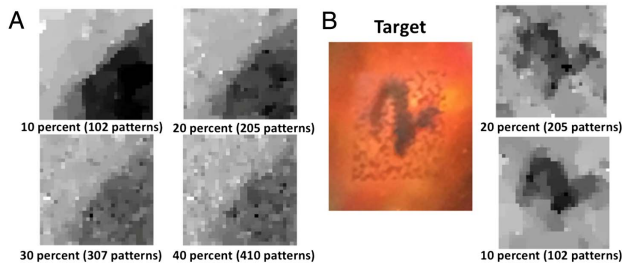

Fig. 3. CS-reconstructed images of (A) edge mask and (B) patterned hydrocarbon target (corresponding target image: black ink on glass) at different percentage pattern recovery (compression rates).

rate. The contrast is improved at higher compression rates (low percentage pattern recovery); however, the spatial details of the mask are more accurately resolved at lower compression rates.

In Fig. 3B, we evaluate the capability of the reconstruction algorithm on the system for image recovery of a patterned hydrocarbon target (character written in ink on glass). With the target imaged on the focal plane of the DMD array, successive exposures to a series of binary patterns were employed at 10%–20% pattern recovery. At 20%, the features of the recovered image are a better representation of the original image compared to the reconstruction at a higher compression rate (10%). The image reconstruction could be further enhanced with lower compression rates; however, 20% recovery is sufficient to recover the required spatial information. Intuitively, for hydrocarbon targets with more complex and heterogeneous chemical spatial distributions, increasing the number of measurements (low compression rate) can be employed to increase the accuracy of image reconstruction.

Now, we investigate the chemical specificity of the SWIR/NIR-CS imaging system for hydrocarbons. In contrast to a single-pixel CS camera, the present system simultaneously records data from 256 compressive pixel detectors, thus enabling the parallel acquisition of spectral data by simultaneously imaging for the SWIR/NIR wavelength range (1000–2000 nm). The components were intentionally marked with distinguishable contrast to aid in visualization of the chemical components (in this case, the chemical composition of the red and green ink on a glass substrate). Commercially available permanent marker inks for red and green colors typically consist of hydrocarbon mixtures of organic pigments, dyes, and volatile alcohols (i.e., butanol and diacetone alcohol). These also contain trace amounts of toxic benzene derivatives such as xylene and cresol. By defining the groups of detector pixels that represent spectral signatures specific to each of the color components, the spectral selectivity of the image reconstruction can be demonstrated. The spectral plot is divided into three discrete regions where each represents various responses from the chemical components and the background artifacts as represented in the raw target image. Depending on the NIR wavelength being probed, hydrocarbon targets that strongly absorb NIR light can be highlighted against the spectrally less-responsive background (wavelength region I in Fig. 4). Region I show negligible response in the CS reconstructed image for both red and green ink components. Region II shows preferential sensitivity to the

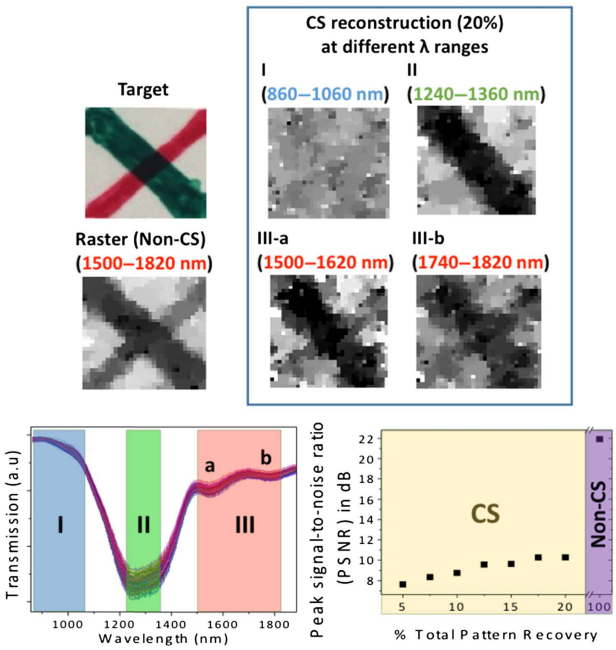

Fig. 4. Raster (non-CS) image versus CS-reconstructed image of two-component target on glass for total transmission intensity at λ range: 1500–1820 nm. The CS-reconstructed images are reconstructed at various wavelength regions (labeled as I, II, and III) showing chemical specificity to the two dyes. For a quantitative comparison of the image quality, the peak signal-to-noise ratio (PSNR) is introduced as figure of merit.

green ink component as shown from the CS-reconstructed image where the red ink is markedly invisible. Region III demonstrates chemical sensitivity for both red and green ink components as seen in the pictorial target image.

In terms of reconstruction quality, we compared the CS results in Fig. 4 to the raster-scan (non-CS) results by introducing quantitative terms as figures of merit. The mean square error (MSE) and the peak signal-to-noise ratio (PSNR) are defined as the following:

$$\mathrm{MSE} = \frac{1}{q_1 q_2} \sum_{i,j=1}^{q_1 q_2} [T_0(i,j) - \tilde{T}(i,j)]^2, \quad (1)$$

$$\mathrm{PSNR} = 10 \log \frac{255^2}{\mathrm{MSE}}. \quad (2)$$

From these equations, T_0 stands for the original scene image consisting of 32×32 pixels while $\tilde{T}$ represents the reconstructed image. In general, a larger PSNR value suggests a better reconstruction result of the actual scene. In Fig. 4, the PSNR of the non-CS reconstructed image is comparably higher (by ~10 dB) to the CS results at 20% ($M = 0.2N$) CS reconstruction. The PSNR of the CS reconstructed image is incrementally improved with a compression rate from 5% ($M = 0.05N$) to 20% ($M = 0.2N$) CS reconstruction. However, for the non-CS image, it was reconstructed from 1024 measurements that requires, in this case, at least 80% more time for the image acquisition process compared to

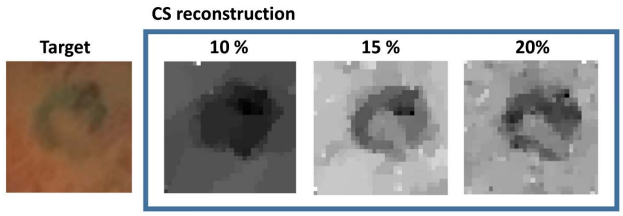

Fig. 5. CS-reconstructed image of crude oil film deposited on glass at different percentage pattern recovery (λ range: 1500–1820 nm).

the CS results at 20% pattern recovery. In contrast to raster-scanning methods, the hyperspectral CS reconstruction results in a faster imaging method for hydrocarbon response in the NIR wavelengths. This will prove to be considerably advantageous for rapid field spectral imaging that requires both chemical specificity and spatial information.

The applicability of the CS-SWIR/NIR system for chemical sensing of hydrocarbon composites in petroleum products (crude oil, Louisiana sweet) is shown in Fig. 5. The SWIR/NIR spectral range is particularly interesting for analysis of crude oil hydrocarbon composition. The absorbance measurements between 1000–2500 nm are particularly relevant to the distinct oil absorption bands of oils rich in asphaltene group components. The oil absorption bands in this region are composed of the vibration combination modes of the C–H bonds (2200–2500 nm) and overtones of C–H bonds (1100–1800 nm) [19,24]. The image reconstruction accuracy increases as the M value increases (lower compression rate). Here, by using fewer measurements (high compression rates, $M \leq 0.20N$), the spatial features (local distribution on the glass substrate) are efficiently represented without relying on time-consuming raster-scanning methods. The demonstration of hydrocarbon detection to provide spatial distribution of hydrocarbons is particularly crucial for immediate identification of crude oil spills in offshore locations. With CS reconstruction, faster SWIR/NIR imaging acquisition can be achieved without the need for expensive large-format 2D pixel detector arrays, advantageous for creation of a cost-effective chemical sensing instrumentation for hydrocarbon detection and identification. Compared to existing CS snapshot configurations that require large format detector arrays, [11,16] the optical architecture of the CS-SWIR/NIR system requires only a 1D array detector. In terms of cost per pixel, the system is an attractive alternative to 2D array detectors with its high costs determined by the overall pixel count and pixel readout speed.

Within the SWIR/NIR spectral range, many absorption spectral signatures can be found. For example, the overtone and combination bands of the C–H, O–H, N–H, S–H, and C–O stretching vibrations are all detectable within the 900–2500 nm range. Our group has a particular interest in imaging hydrocarbons in various spectral bands for potential stand-off detection and *in situ* monitoring of offshore oil spills. In addition, we have modeled and experimentally verified thickness-induced IR contrast of oil film on the water surface [25,26]. Further, we have evaluated a compressed sensing sensor design for detecting thin oil slicks on the water surface [27]. These oil slick signatures can in principle be found in the

SWIR/NIR wavelength range. For building a field prototype, size and power consumption need to be considered. For our present configuration, the total power can be well below 500 W. The size of the prototype will be dictated by the relaying optics and imaging systems. With careful design, the entire system can be fit into a box $\sim$1 ft^3.

4. CONCLUSION

In conclusion, we presented a new approach for hyperspectral SWIR/NIR imaging using a DMD and line-array detector to simultaneously provide spatial and spectral information. The CS imaging in the SWIR/NIR wavelengths provides a cost-effective alternative to existing sensors using large format pixel array detectors. The optical architecture demonstrated here is generally adaptable to other spectral regimes such as the mid-IR and thermal imaging range. The absence of mechanical moving parts (scanning diffraction gratings, galvomirrors, etc.) makes it advantageous for field applications. The CS scheme allows one to flexibly trade image quality for acquisition speed. For future work, improvements on the light-throughput conditions of the SWIR/NIR sensor can significantly enhance the PSNR of the reconstructed images, further reducing the noise gap with the raster-scanning results. The multiaperture settings of the DMD modulator can be also further customized to increase image resolution and enhance parallel-spectral image reconstruction. It can be further integrated with a modified CS algorithm that utilizes deliberately selective mechanisms in generating modulation patterns (sample-specific based on *a priori* information) that will further reduce acquisition time (higher compression rates). Moreover, when it comes to the use of fiber optical materials, constructing a hyperspectral sensor for the SWIR/NIR window does not have problematic material absorption limitations typical in mid-IR applications. Thus, remote sampling using fiber optical sensing can be readily integrated in future modifications, further increasing the applicability for field sampling.

Funding. National Science Foundation (NSF) (1151154, 1605683).

REFERENCES

1. M. Jamrógiewicz, "Application of the near-infrared spectroscopy in the pharmaceutical technology," J. Pharmaceutical Biomed. Anal. **66**, 1–10 (2012).
2. G. Elmasry, M. Kamruzzaman, D.-W. Sun, and P. Allen, "Principles and applications of hyperspectral imaging in quality evaluation of agro-food products: a review," Crit. Rev. Food Sci. Nutr. **52**, 999–1023 (2012).
3. M. Blanco, M. Alcalá, J. Planells, and R. Mulero, "Quality control of cosmetic mixtures by NIR spectroscopy," Anal. Bioanal. Chem. **389**, 1577–1583 (2007).
4. M. Sowa, J. Friesen, M. Levasseur, B. Schattka, L. Sigurdson, and T. Hayakawa, "The utility of near infrared imaging in intra-operative prediction of flap outcome: a reverse McFarlane skin flap model study," J. Near Infrared Spectrosc. **20**, 601–615 (2012).
5. W.-C. Shih, K. L. Bechtel, M. S. Feld, M. A. Arnold, and G. W. Small, *Introduction to Spectroscopy for Noninvasive Glucose Sensing, In Vivo Glucose Sensing* (Wiley, 2009), pp. 331–356.
6. J. Workman, "Review: a brief review of near infrared in petroleum product analysis," J. Near Infrared Spectrosc. **4**, 69–74 (1996).
7. J. Qi and W.-C. Shih, "Performance of line-scan Raman microscopy for high-throughput chemical imaging of cell population," Appl. Opt. **53**, 2881–2885 (2014).
8. D. Xiang and M. A. Arnold, "Solid-state digital micro-mirror array spectrometer for Hadamard transform measurements of glucose and lactate in aqueous solutions," Appl. Spectrosc. **65**, 1170–1180 (2011).
9. J. D. Batchelor and B. T. Jones, "Development of a digital micromirror spectrometer for analytical atomic spectrometry," Anal. Chem. **70**, 4907–4914 (1998).
10. H. Liu and B. Bhushan, "Nanotribological characterization of digital micromirror devices using an atomic force microscope," Ultramicroscopy **100**, 391–412 (2004).
11. H. Chen, M. S. Asif, A. C. Sankaranarayanan, and A. Veeraraghavan, "FPA-CS: focal plane array-based compressive imaging in short-wave infrared," in *IEEE Conference on Computer Vision and Pattern Recognition (CVPR)* (2015), pp. 2358–2366.
12. J. E. Fowler, "Compressive pushbroom and whiskbroom sensing for hyperspectral remote-sensing imaging," in *IEEE International Conference on Image Processing (ICIP)* (2014), pp. 684–688.
13. R. Bhargava, "Infrared spectroscopic imaging: the next generation," Appl. Spectrosc. **66**, 1091–1120 (2012).
14. W. G. Fateley, R. M. Hammaker, R. A. DeVerse, R. R. Coifman, and F. B. Geshwind, "The other spectroscopy: demonstration of a new de-dispersion imaging spectrograph," Vib. Spectrosc. **29**, 163–170 (2002).
15. Z. Sadeghipoor, Y. M. Lu, and S. Süsstrunk, "A novel compressive sensing approach to simultaneously acquire color and near-infrared images on a single sensor," in *IEEE International Conference on Acoustics, Speech and Signal Processing* (2013), pp. 1646–1650.
16. M. F. Duarte, M. A. Davenport, D. Takhar, J. N. Laska, T. Sun, K. E. Kelly, and R. G. Baraniuk, "Single-pixel imaging via compressive sampling," IEEE Signal Process. Mag. **25**, 83–91 (2008).
17. D. Takhar, J. N. Laska, M. B. Wakin, M. F. Duarte, D. Baron, S. Sarvotham, K. F. Kelly, and R. G. Baraniuk, "A new compressive imaging camera architecture using optical-domain compression," Proc. SPIE **6065**, 606509 (2006).
18. D. Xiang and M. A. Arnold, "Chemical imaging with a solid-state near infrared spectrometer based on a digital micro-mirror array device coupled with Hadamard transform spectroscopy," Anal. Lett. **45**, 1070–1078 (2012).
19. E. A. Cloutis, "Spectral reflectance properties of hydrocarbons: remote-sensing implications," Science **245**, 165–168 (1989).
20. C. Burgess and J. Hammond, "Wavelength standards for the near-infrared spectral region," Spectroscopy **22**, 40–47 (2007).
21. E. J. Candè and M. B. Wakin, "An introduction to compressive sampling," IEEE Signal Process. Mag. **25**, 21–30 (2008).
22. Z. Han, H. Li, and W. Yin, *Compressive Sensing for Wireless Networks* (Cambridge University, 2013).
23. E. J. Candes and T. Tao, "Information theory, near-optimal signal recovery from random projections: universal encoding strategies?" IEEE Trans. Inf. Theory **52**, 5406–5425 (2006).
24. C. Pasquini and A. F. Bueno, "Characterization of petroleum using near-infrared spectroscopy: quantitative modeling for the true boiling point curve and specific gravity," Fuel **86**, 1927–1934 (2007).
25. W.-C. Shih and A. B. Andrews, "Modeling of thickness dependent infrared radiance contrast of native and crude oil covered water surfaces," Opt. Express **16**, 10535–10542 (2008).
26. W.-C. Shih and A. B. Andrews, "Infrared contrast of crude-oil-covered water surfaces," Opt. Lett. **33**, 3019–3021 (2008).
27. Y. Li, W.-C. Shih, Z. Han, and W. Yin, "Oil spill sensor using multispectral infrared imaging via l1 minimization," in *IEEE International Conference on Acoustics, Speech, and Signal Processing (ICASSP)*, Prague, Czech Republic, 2011.